POAC'25
St. John's, Newfoundland and Labrador, Canada

Proceedings of the 28th International Conference on Port and Ocean Engineering under Arctic Conditions
Jul 13-17, 2025
St. John's, Newfoundland and Labrador Canada

Improved melt pond automatic extraction algorithm for oblique shipborne imagery

Jiaru Zhou[1], Qinkai Wang[1], Peng Lu[1], Qin Zhang[2], Li Zhou[3]
[1] State Key Laboratory of Coastal and Offshore Engineering, Dalian University of Technology, Dalian 116023, China
[2] Ice Service, Norwegian Meteorological Institute, N-9293 Tromsø, Norway
[3] School of Ocean and Civil Engineering, Shanghai Jiao Tong University, Shanghai 200240, China

ABSTRACT

In summer Arctic, due to its ability to reduce the overall albedo of the ice surface, melt pond is an important feature for the mechanism study of sea ice surface melting. Currently, satellite remote sensing is main method of obtaining sea ice and melt pond in large scale, while the high-resolution shipborne optical images captured in situ reflect the "ground truth" of sea ice surface, served as an important supplement to satellite remote sensing. However, methods to automatically extract spatially distributed melt pond from a large shipborne sea ice imagery set still need to be developed. This article proposed an improved automated extraction scheme for ice surface features in shipborne imagery, named Oblique Ice Surface Features Automatic Extraction algorithm (O-ISFAE). The principles of Random Forest, Watershed Transformation and orthographic correction were utilized in this scheme. First of all, we elaborated on the working mechanism of the O-ISFAE algorithm. Then, taking CHINARE-2018 shipborne imagery set as an application example, a training set (SSITS-2018) was created, and then a Random Forest classification model (SSIRF-2018) was constructed. Finally, the classification accuracy and applicability on CHINARE-2018 were tested with manual results as validation data. This study would play an important role in promoting the automated extraction of melt pond from high-resolution optical shipborne images in the future.

KEY WORDS: Random forest; Arctic sea ice; Melt pond; Image processing

1 Introduction

Melt pond is one of the most significant surface features in summer arctic, and plays an important role in ice surface albedo feedback [1-4]. Therefore, it is crucial to extract spatial distribution of melt ponds on ice surface for the studies of the mechanism of arctic sea ice melting mechanism. At present, the observations on sea ice and melt pond mainly rely on satellite remote sensing [5-10]. However, limited by cloud cover and similar brightness temperature characteristics [11], there were still certain biases and limitations in the retrieval on sea ice and melt pond with numerous efforts have done [12-17]. In the meantime, "ground truth" could effectively serve as validation and supplementary data for passive microwave retrieval, and even correct deviations caused by melt pond [18]. In addition to arriving at the

melt pond surface for measurement, in-situ observations were also carried out by helicopter & and aerial photography (less than 500m above the sea) [4, 19-24] and shipborne photography (less than 25m above the sea) [18, 25, 26]. Although limited field of view leads to sampling bias, its typical sub-meter high-spatial resolution makes it possible to realize detailed and accurate estimates of melt ponds (especially below 200 m^2).

At present, automatically extracting ice surface features, especially melt ponds, re-mains a technical problem [27]. Methods for distinguishing ice and water appeared relatively mature, including local thresholding [28], image analysis tool ASIS[29] and a series of image processing technologies under the framework of ARKTOS[30]. For melt ponds in sRGB images, the previous thresholding methods for gray-scale images are no longer available because of the injection of bluish components. Currently, methods for melt pond identification mainly based on two principles. One is based on red-green-blue (RGB) component [31], according to two facts: (1) melt ponds in aerial images usually appear blue, while ice and water appear white and black, respectively [32]; (2) compared with the ice, melt pond has higher brightness in blue component than in red component [33]. The manually supervised Band-Thresholding method (BT) adopted in CHINARE-2008 aerial images is also belongs to this kind of principle [18]. BT method, benefits from the ad-vantages of naked eyes, is widely applied in Chinese National Arctic Research Expeditions (CHINAREs) [32-36]. The other is the classification based on pattern recognition, in which texture features, such as intensity and variance, of each image are calculated, and then a neural network [3] or a discriminant function [37] is determined using a training set formed by manual classification of images, then other images can be processed automatically by the trained network or function. In addition, in the Random Forest Classification model of the OSSP algorithm [38], a combination of attributes that describe the intensity and textural characteristics were selected, simultaneously integrated two principles mentioned above. Melt ponds were successfully extracted from four orthographic sea ice imagery resources (including high-resolution imagery from IceBridge (SIZRS) and UAVs, panchromatic and multispectral imagery from satellite imaging bandwidth (DigitalGlobe WorldView 4)) in the original OSSP algorithm, but not including oblique imagery. Among these methods, the recognition by naked eyes is still the optimal in accuracy, like the BT method. But its application in CHINAREs was still not well enough for its drawbacks like extremely low efficiency and utilization rate, as well as sampling errors. Therefore, our goal is to develop an automated scheme with accuracy comparable to naked eye, which can batch process high-resolution shipborne oblique sea ice optical imagery of various ice conditions in the meantime.

To address the issues mentioned above, a scheme (Oblique Ice Surface Features Automatic Extraction algorithm (O-ISFAE)) based on theories of previous studies was pro-posed in this paper. Firstly, in Section 2, we introduced the method framework of the O-ISFAE algorithm, and then elaborated the training method on shipborne sea ice imagery set. Secondly, the results of the O-ISFAE algorithm were stated in Section 3. Finally, the conclusions and limitations of the O-ISFAE algorithm were discussed in Section 4.

2. Method

2.1. Method Framework

The flowchart of the scheme proposed in this paper was shown in Figure 1. This scheme was logically based on theoretical framework of the OSSP algorithm, but improved to be suitable for complicate shipborne sea ice imagery set, named the Oblique Ice Surface Features

Automatic Extraction algorithm (O-ISFAE). There were three improvements were mainly made: firstly, the open-source codes were reorganized and modified and threshold values in training were resettled; secondly, a new definition called training set unit (TSU) was put forward and a process of selecting and merging was added; thirdly, orthographic correction was implemented after random forest classification. The pseudocode for the main algorithm process was shown in Algorithm 1.

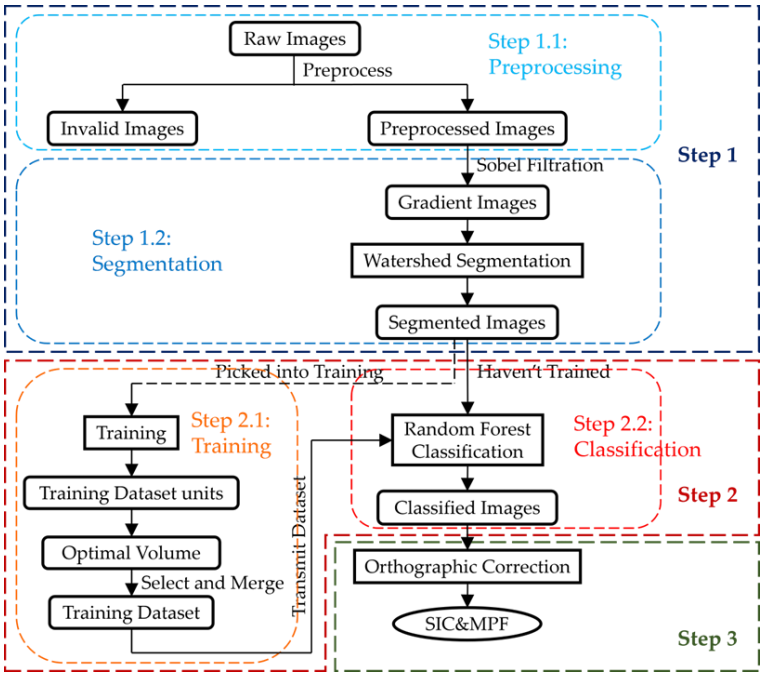

Figure 1. Flowchart of the O-ISFAE algorithm.

Algorithm 1 O-ISFAE.

PRE ← Preprocess

B ← Binary Image convertion from **PRE**

G ← $$G = \sqrt{G_x^2 + G_y^2}, G_x = \begin{bmatrix} -3 & 0 & +3 \\ -10 & 0 & +10 \\ -3 & 0 & +3 \end{bmatrix} * \boldsymbol{B}, G_y = \begin{bmatrix} -3 & -10 & -3 \\ 0 & 0 & 0 \\ +3 & +10 & +3 \end{bmatrix} * \boldsymbol{B}$$

S ← Region Seed of **B,** the regional minimum calculated from **G**

SEGMENTATION ← Watershed Transformation based on **G** and begin with **S**

TS ← Training Set creation (**Algorithm 2**)

CLASSIFICATION ← Random Forest Classification based on **TS**

RWB ← Image with classified label (Red-OW, White-S&I, Blue-MP)

O-RWB ← Orthographic Correction on **RWB** (**Algorithm 3**)

SIC/MPF ← derived from **O-RWB**

return SIC/MPF

2.2. Procedure

2.2.1. Step1: Preprocessing and Segmentation

The results on every stage of the O-ISFAE algorithm was shown in Figure 2. The first step was preprocessing (Step 1.1). When we obtained the original imagery set, parts of imagery set were firstly excluded through visual browsing, as shown in Figure 2a and 2b. These excluded images referred to those affected by uneven illumination, distortion and other objective factors, which called invalid images. In these images, Sea ice surface information was corrupted or covered up. Then white balancing, contrast enhancing and moderate sharpening were implemented on valid images. The preprocessed shipborne image was shown in Figure 2c.

Then we segmented the preprocessed image (Step 1.2). Before watershed segmentation, the preprocessed image was converted into the binary image, as shown in Figure 2d. Then the Sobel edge detection helped retrieving the boundaries between ice-water, ice-melt pond and melt pond-water. Based on the boundaries, gradient imageries were generated, as shown in Figure 2e. Gradient was meant to finding the local minimum points as original points in watershed segmentation. As shown in Figure 2f, watershed segmentation showed its robust and made a success on preprocessed oblique shipborne imagery. We found noises on ice floes, weak boundaries formed due to perspective of distant small regions, were ignored in watershed segmentation. This kind of noises were rare in orthographic imagery, but were common in shipborne imagery.

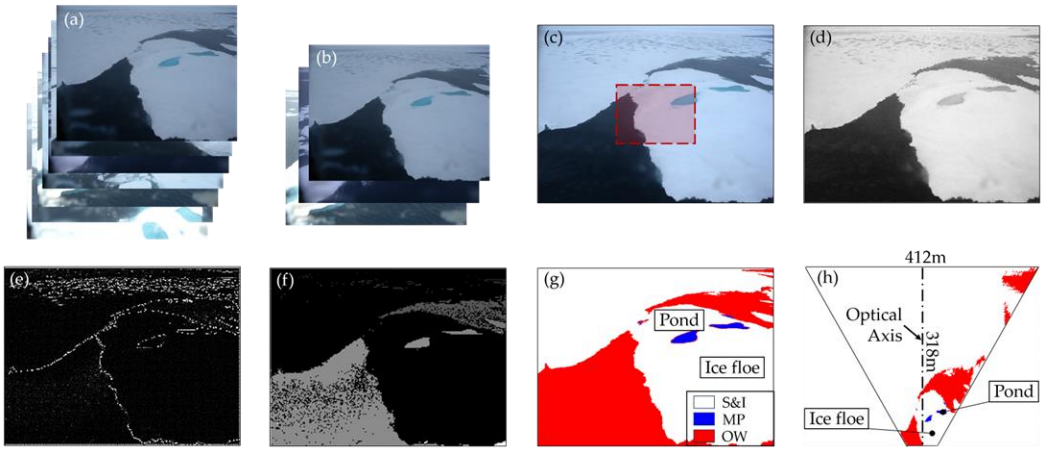

Figure 2. The result example of each stage of the O-ISFAE algorithm during shipborne image processing. (a) was raw shipborne sea ice imagery set. (b) was valid shipborne imagery set. (c) was a pre-processed shipborne image, in which the red dotted rectangle area was selected for training. (d) was the binary image. (e) was the gratitude image. (f) was the segmented image. (g) tricolor classified image with color labels, in which white represented S&I, blue represented MP, and red represented OW. (h) was the trapezoidal tricolor image after orthographic correction of (g), with the true dimensions marked. In addition, ice floe and melt pond example were annotated, as well as their positions before and after orthographic correction.

2.2.2. Step2: Training and Classification

Training (Step 2.1) was the most important in the algorithm, because it would deter-mine the accuracy of classification. In training, supervisors need to determine each of the segmented object into three surface types: snow and ice (S&I), melt pond (MP) and open water (OW). Before determination, the relevant attributes of objects were calculated. After testing, the attributes of high contribution in shipborne imagery were found similar to those of aerial sRGB images, which were listed in Table 1.

Table 1. The attributes selected for training in shipborne sea ice imagery.

R band	G band	B band	RGB variant	Image intensity
Mean* SD*	Mean* SD*	Mean* SD*	(B - R)/(B + R)** (B - G)/(B + G)** (G - R)/(2•B - G - R)**	Entropy*

* Nicholas C. Wright et al. (2018) [38]; ** Miao et al. (2015) [39]

To reduce unnecessary workload and further improve training efficiency, a single training set volume threshold of 1000 was set, which means classifying 1000 objects ended a training session. The generated single TS of 1000 was called a training set unit (TSU). This would increase the degree of freedom, allowed us to recombine and translate different TSUs as needed, for testing the accuracy of TS with various combination of TSUs. And it had been proven that, within a certain range, the more interested objects contained in training, the better the classification effect was. Therefore, we could try to select one of the sub-images containing MP for training, as shown in Figure 2c)

The pseudocode for the training algorithm process was shown in Algorithm 2. Based on the generated classifier, all objects segmented from the image set could be classified (Step 2.2). After RF classification, a tricolor classified image with color labels was obtained, as shown in Figure 2b. White represented S&I, blue represented MP, and red represented OW.

Algorithm 2 Training Set Creation.

GUI ← the Graphical User Interface to classify unknown objects

TSU ← training set unit of 1000 classified objects

TS ← recombine and translate the **TSU**s together

return TS

2.2.3. Step3: Orthographic Correction and Calculation

It should be noted that when photographing at an angle, the pixel fraction in Figure 2b was not the true area fraction. To extract the correct ice surface feature parameters, geo-metric correction was required on the tricolor classified images. The pseudocode for the geometric correction algorithm process was shown in Algorithm 3. The result after geometric correction was shown in Figure 2d.

The size of image (m ×n), equivalent focal length (f) and equivalent photo size (ps) were decided by CCD sensor. The height of camera (h) and incline angle of lens (a) were

determined as soon as the CCD sensor was settled. Then the row and column resolution was calculated. In this way, the coordinates on sea ice surface (xx, yy) and actual area of each pixel were able to be calculated from image coordinates (x, y) by the formats[40] in Algorithm 3. It is worth noting that the true area of each row of pixels was the same for the Centered optical axis of lens, as the dotted line shown in Figure 2d. Besides, the top 300 rows of pixels in the image were excluded from the calculation due to severe distortion.

The true size of the trapezoidal field of view had been calibrated, and the true area was 73935m2. Once the geometric correction was completed, the ice surface feature parameters of interest, like sea ice concentration (SIC) and melt pond fraction (MPF), were able to be extracted. SIC is defined as the ratio of the sum of the areas of S&I and MP (the sum of the red and blue areas in (d)) to the entire trapezoidal area, while MPF is defined as the ratio of the area of MP (the blue area in (d)) to the entire trapezoidal area.

Algorithm 3 Orthographic Correction.

m,n ← size of image m ×n

thN ← row number less than thN are excluded

h ← height of camera from sea surface(m)

f ← equivalent 35mm focal length(m)

a ← incline angle of lens(radians)

ps ← equivalent 35mm photo size(m)

rr,cr ← $rr = ps(row)/m, cr = ps(col)/n$

R/W/B ← generates a binary image with a foreground color of OW/S&I/MP

x,y ← image coordinates x,y

xx,yy ← $yy(i,j) = h \times \tan(a + \arctan(y/f))$

$$xx(i,j) = x \times \sqrt{(h^2 + yy(i,j)^2)/(f^2 + y^2)} \quad \textbf{for } i = 1, \dots, m;\ j = 1, \dots, n$$

dx,dy ← $dy(i) = rr \times h/f/\cos^2(a + \arctan(y/f))/(1 + (y/f)^2)$

$$dx(i) = cr \times \sqrt{(h^2 + yy^2)/(f^2 + y^2)} \quad \textbf{for } i = 1, \dots, m$$

dxy ← $dxy(i) = dx(i) \times dy(i)$ **for** $i = 1, \dots, m$

O-RWB ← generate Orthographic Corrected RWB image

return O-RWB

3. Results

With SSIRF-2018, we test the applicability of SSIRF-2018 on SSIIS-2018. In the test, 500 images were randomly selected from SSIIS-2018 as a sample (S), representing the composition of the entire SSIIS-2018. Six categories of images were summarized through visual interpretation. The composition of the entire SSIIS-2018 could be inferred based on the proportion of images in each category in S. Extracted a certain number of images from each of the six categories as test set samples (TSs I-VI). Then evaluated the comprehensive

performance of SSIRF-2018 on TSs I-VI.

Considering the proportion of S&I, MP, and OW, as well as the relationship between ice surface conditions and other surface types, all images in S could be divided into the six categories as following:

1. Category I: S&I+MP (Snow, Ice and Melt Pond). There was only snow, ice and melt ponds (occupy about 10% in S);

2. Category II: S&I+MP+OW (Snow, Ice, Melt Pond and Open Water). The three main ice surface types were all exit at the same time, which was the most common case (about 50% in S);

3. Category III: S&I+OW (Snow, Ice and Open Water). There was only snow, ice and water (about 30% in S).

4. Category IV: S&I+SI+OW (Snow, Ice, Submerged Ice and Open Water). There was typical submerged ice, one side of which was ice and the other side was water (about 4% in S);

5. Category V: S&I+MTP+OW (Snow, Ice, Melt-Through Pond and Open Water). This kind of image contained many melt ponds, but almost were melt-through ponds, whose color were similar to open water (about 4% in S);

6. Category VI: C-CI&TP (Complex-Crushed Ice, Tiny Pond and Open Water). These images were tough to process, not only by algorithm, but also by human. There were large areas of brush ice and many very small melt ponds, which made ice surface over-complicated (about 2% in S).

Table 2. The actual area proportions of S&I, MP, and OW extracted from typical images of six categories (Category I-VI) using BT method and the O-ISFAE algorithm. ΔI, ΔP and ΔW represented the difference between BT and O-ISFAE results, respectively.

Category	**Time(d/m/yh/m)**	**Latitude(℃), Longitude(℃)**	**Method**	**S&I (%)**	**ΔI (%)**	**MP (%)**	**ΔP (%)**	**OW (%)**	**ΔW (%)**
Category I	02/08/2018 19:33	74.62, 168.10	BT	92.5	1.1	4.6	-0.8	2.9	-0.3
			O-ISFAE	93.6		3.8		2.6	
Category II	09/08/2018 03:03	77.76, 157.34	BT	86.5	-1.0	0.3	-0.1	13.2	1.1
			O-ISFAE	85.5		0.2		14.3	
Category III	26/08/2018 14:36	83.63, 159.79	BT	98.4	0.2	0.0	0.0	1.6	-0.2
			O-ISFAE	98.6		0.0		1.4	
Category IV	26/08/2018 16:01	83.53, 159.94	BT	75.3	2.3	0.3	-0.2	24.4	-2.1
			O-ISFAE	77.6		0.1		22.3	
Category V	11/08/2018 01:48	79.25, 168.87	BT	61.5	-0.1	0.2	-0.2	38.3	0.3
			O-						

			ISFAE	61.4		0.0		38.6	
Category VI	01/08/2018 16:18	74.84, 159.16	BT O-ISFAE	64.4 64.6	0.2	0.5 0.2	-0.3	35.1 35.2	0.1

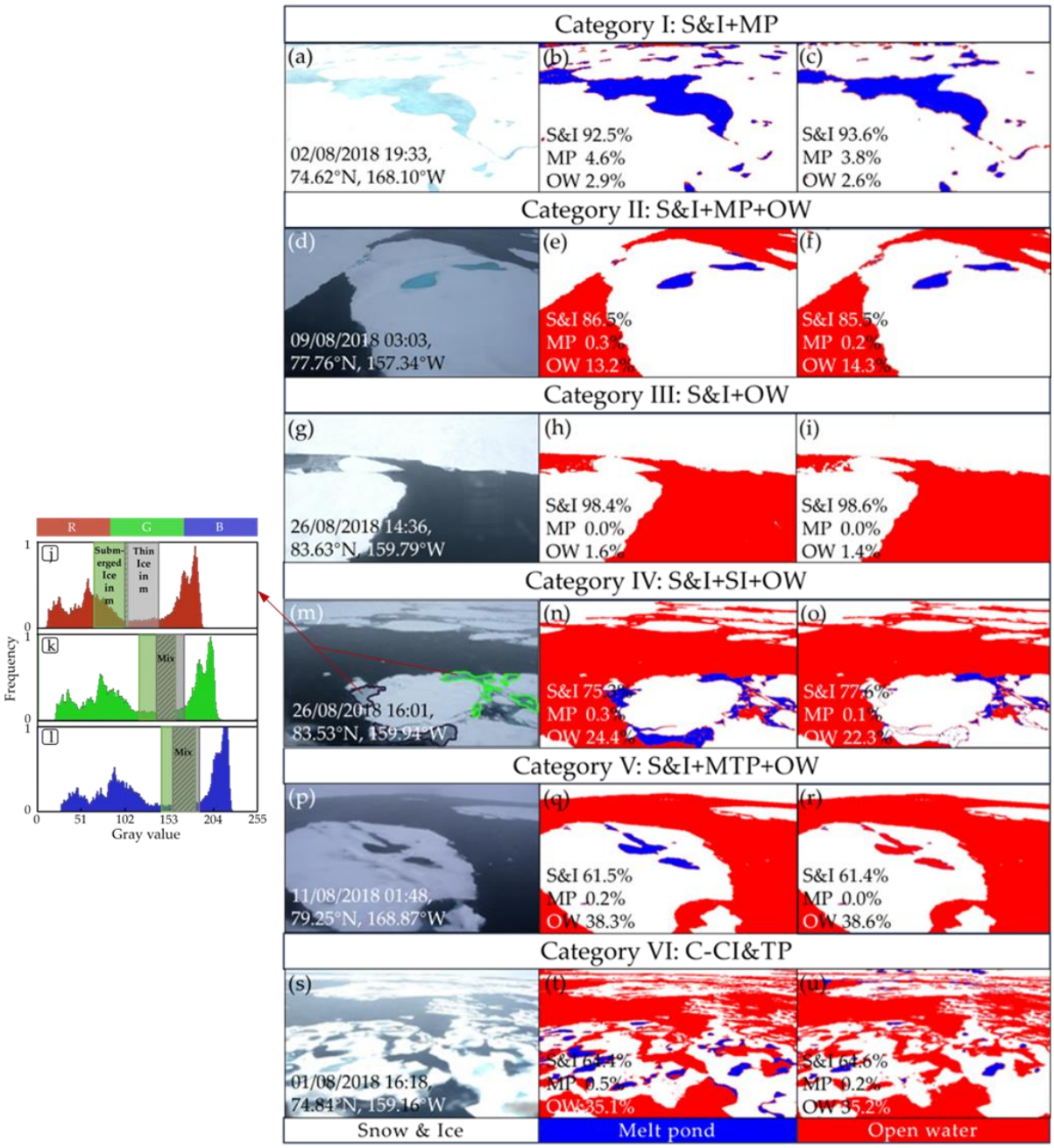

Figure 3. Typical images ((a), (d), (g), (m), (p), (s)) of six categories (Category I-VI) were processed using BT method ((b), (e), (h), (n), (q), (t)) and O-ISFAE algorithm ((c), (f), (i), (o), (r), (u)), respectively. In addition, spatiotemporal information was annotated in typical images, and the actual area proportions of S&I, MP, and OW were annotated in the tricolor images. (j-

l) were the gray level histogram of RGB channel of (m), and the dark gray and green rectangle shadows in (j-l) represented the gray line and green line region in (m). These two regions were transition types, the green line region was similar to SI and the gray line region was similar to TI, significantly the mix area reported the overlap interval of gray value of two transition types in RGB channel.

Each representative image was selected from six categories and then was processed by BT method and the O-ISFAE algorithm, as shown in Figure 3a-I and m-u. Intuitively, the O-ISFAE algorithm could accurately classify S&I, MP, and OW in Category I-III, as shown in Figure 3a-i. However, the classification accuracy of Category IV-VI was slightly poor, as shown in Figure 3m-u. In addition, to quantify the classification results, we calculated the actual area proportions of S&I, MP, and OW in the tricolor images, and calculated the differences, as ΔI, ΔP and ΔW in Table 2. If ranking six categories based on ΔI, ΔP and ΔW by low to high, Category III was the first with the integrated minimum of ΔI 0.2% and ΔW -0.2%, which indicated that the O-ISFAE algorithm could effectively classify S&I and OW in shipborne images, as shown in Figure 3g-i. Next category was Category VI, followed by Category V, Category I, Category II, and Category IV. Although Category VI and Category V were ranked before Category I and Category II, it was evident that the classification results were not as accurate as the latter two categories. This was because the difference was mainly in the MP, and the proportions of the MP after geometric correction was very small, even two orders of magnitude different from those of S&I and OW. The surface conditions in Category VI were complex, and even the BT method under manual supervision was difficult to handle, as shown in Figure 3s. Due to limited image information, some areas were difficult to determine which main surface type they belong to. In this case, although the difference in MP was small as -0.3%, the visual comparison in Figure 3t and u could better show the differences in detail between two methods. As for Category V, there was a typical MTP, as shown in Fig. 3(p). The BT method could label the MTP with manual supervision, but in the automated O-ISFAE algorithm MP and OW could not be distinguished, resulting in an underestimation of MP by 0.2%, as shown in Figure 3q and r. Category I had a maximum difference of 1.1% on S&I, which slightly overestimated by the O-ISFAE algorithm, while underestimating 0.8% on MP. It was observed that few pixels were classified as OW in Category I, in which S&I and OW were mainly focused on, thus belonged to noise, as shown in Figure 3b and c. Category II contains three main surface types, and the results showed a relatively large difference of -1.0 and 1.1 on S&I and OW, respectively. In contrast to Category I, it slightly underestimated S&I and slightly overestimated OW, as shown in Figure 3e-f. The difference on MP was not significant between Category I and Category II, in both of which MP were slightly underestimated by the O-ISFAE algorithm. Category IV did not have a typical MP, but there was obvious SI, as shown in Figure 3m. As explained in Section 3, SI was also classified to MP. The O-ISFAE algorithm classified less SI than the BT method, resulting in an underestimation of 0.2% in MP, as shown in Figure 3n and o. This was because some surfaces were in the transition period from dark TI to blue SI. When querying the channel grayscale values, it was found that the grayscale interval overlapped severely and the optical feature differentiation was not clear. The overlapping interval corresponded to the RGB channel (R 103-113, G 137-159, B 156-180), as shown in the mix section of Figure 3j-l. When approaching TI, it was classified to S&I in the O-ISFAE algorithm, while when approaching SI, it was classified to MP. However, this kind of surface types in transition could be recognized in the BT method with manual supervision, by visually interpreting in conjunction with the ice surface conditions in the image. Overall, for Category I-III, the

results calculated by the O-ISFAE algorithm were highly consistent with the BT method results, with the highest difference not exceeding 1.1%. For Category IV and Category V, the results calculated by the O-ISFAE algorithm were basically consistent with the results of the BT method, with the highest difference not exceeding 2.3%. For Category VI, although the difference was not significant, the ice conditions were too complex, and both methods had poor effects, which had low reference significance.

In addition, six confusion matrices were drawn to evaluate the classification accuracy of the O-ISFAE algorithm on typical images of six categories, and further indicators were calculated to quantify the evaluation of classification accuracy.

4. Conclusions

Based on theories of the OSSP algorithm proposed by Nicholas C. Wright et. al. [38], a scheme towards shipborne imagery, Oblique Ice Surface Features Automatic Extraction algorithm (O-ISFAE), was proposed in this paper. Taking the CHINARE-2018 shipborne image set as an example, the optimal volume of training set was determined to be 84000 based on the variation of six parameters. We created a personalized training set SSITS-2018 and constructed a RF model SSIRF-2018 with 100 decision trees and unlimited depth extension.

Six categories of images were summarized from the CHINARE-2018 shipborne image set. The classification accuracy and applicability of SSIRF-2018 on these six categories of images were tested and evaluated. Using the BT method results as validation data, in or-der to quantify the comparative analysis results, confusion matrices were drawn and multiple secondary and tertiary evaluation indicators were calculated. It was found that ACC and κ of Category I-III, totally accounting for 90% of the CHINARE-2018 shipborne image set, were above 95% and 0.89, respectively. In fact, apart from Category VI (ACC 89%, κ 0.79), all categories ACC and κ reached above 94% and 0.89 respectively. However, Category VI, accounting for less than 2% of the CHINARE-2018 shipborne image set, were also difficult to process by the BT method that rely on human naked eye. It indicated that the results of the O-ISFAE algorithm were highly consistent with those of the BT method, suitable for 98% of CHINARE-2018 shipborne image set. In addition, the processing efficiency of the O-ISFAE algorithm was about 17 times that of the BT method (with an average of 14s/sheet for the O-ISFAE algorithm and 180s/sheet for the BT method).

Future algorithms will not be limited to three surface types: S&I, MP, and OW. Furthermore, they will include shadows (combined with shooting angles and solar zenith angles, which may be used to obtain information on ice ridge heights), submerged ice (boundary of floating ice, distinguished from melt ponds), bright MP (shallower melt ponds), dark MP (deeper melt ponds) and MTP. Extracting these refined surface types from the entire shipborne image set will be a new challenge.

ACKNOWLEDGEMENTS

Support was provided by the National Key Research and Development Program of China (2022YFE0107000).

REFERENCES

Curry, J.A.; Schramm, J.L.; Ebert, E.E. Sea Ice-Albedo Climate Feedback Mechanism. J. Clim. 1995, 8, 240-7.

Diamond, R.; Sime, L.C.; Schroeder, D.; Guarino, M.; Guarino, M. The contribution of melt ponds to enhanced Arctic sea-ice melt during the Last Interglacial. The Cryosphere. 2021, 15, 5099-114.

Pedersen, C.A.; Roeckner, E.; Lüthje, M.; Winther, J.G. A new sea ice albedo scheme including melt ponds for ECHAM5 general circulation model. Journal of Geophysical Research: Atmospheres. 2009, 114, D8101.

Tucker, W.B.; Gow, A.J.; Meese, D.A.; Bosworth, H.W.; Reimnitz, E. Physical characteristics of summer sea ice across the Arctic Ocean. Journal of Geophysical Research: Oceans. 1999, 104, 1489-504.

Cavalieri, D.J.; Parkinson, C.L.; Gloersen, P.; Comiso, J.C.; Zwally, H.J. Deriving long-term time series of sea ice cover from satellite passive-microwave multisensor data sets. Journal of Geophysical Research: Oceans. 1999, 104, 15803-14.

Kern, S. A new method for medium-resolution sea ice analysis using weather-influence corrected Special Sensor Micro-wave/Imager 85 GHz data. Int. J. Remote Sens. 2004, 25, 4555-82.

Markus, T.; Cavalieri, D.J. An enhancement of the NASA Team sea ice algorithm. Ieee Trans. Geosci. Remote Sensing. 2000, 38, 1387-98.

Spreen, G.; Kaleschke, L.; Heygster, G. Sea ice remote sensing using AMSR-E 89-GHz channels. Journal of Geophysi-cal Research: Oceans. 2008, 113, C2S-C3S.

Zhang, S.; Zhao, J.; Frey, K.; Su, J. Dual-polarized ratio algorithm for retrieving Arctic sea ice concentration from passive microwave brightness temperature. J. Oceanogr. 2013, 69, 215-27.

Zhang, S.; Zhao, J.; Li, M.; Liu, S.; Zhang, S. An improved dual-polarized ratio algorithm for sea ice concentration retrieval from passive microwave satellite data and inter-comparison with ASI, ABA and NT2. J. Oceanol. Limnol. 2018, 36, 1494-508.

Fetterer, F.; Untersteiner, N. Observations of melt ponds on Arctic sea ice. Journal of Geophysical Research: Oceans. 1998, 103, 24821-35.

Ding, Y.; Qu, Y.; Peng, Z.; Wang, M.; Li, X. Estimating Surface Albedo of Arctic Sea Ice Using an Ensemble Back-Propagation Neural Network: Toward a Better Consideration of Reflectance Anisotropy and Melt Ponds. Ieee Trans. Geosci. Remote Sensing. 2022, 60, 1-17.

Herzfeld, U.C.; Trantow, T.M.; Han, H.; Buckley, E.; Farrell, S.L.; Lawson, M. Automated Detection and Depth Determi-nation of Melt Ponds on Sea Ice in ICESat-2 ATLAS Data—The Density-Dimension Algorithm for Bifurcating Sea-Ice Re-flectors (DDA-Bifurcate-Seaice). Ieee Trans. Geosci. Remote Sensing. 2023, 61, 1-22.

Makynen, M.; Kern, S.; Rosel, A.; Pedersen, L.T. On the Estimation of Melt Pond Fraction on the Arctic Sea Ice With EN-VISAT WSM Images. Ieee Trans. Geosci. Remote Sensing. 2014, 52, 7366-79.

Rosel, A.; Kaleschke, L. Influence of melt ponds on microwave sensors' sea ice concentration retrieval algorithms.:IEEE, 2012,3261-4.

Scharien, R.K.; Yackel, J.J. Analysis of surface roughness and morphology of first-year sea ice melt ponds: implications for microwave scattering. Ieee Trans. Geosci. Remote Sensing. 2005, 43, 2927-39.

Tanaka, Y.; Scharien, R.K. Potential of Melt Pond Fraction Retrieval From High Spatial Resolution AMSR-E/2 Channels. Ieee Geosci. Remote Sens. Lett. 2022, 19, 1-5.

Wang, Q.; Lu, P.; Zu, Y.; Li, Z.; Leppäranta, M.; Zhang, G. Comparison of Passive Microwave Data with Shipborne Photo-graphic Observations of Summer Sea Ice Concentration along an Arctic Cruise Path. Remote Sens. 2019, 11, 2009.

Holt, B.; Digby, S.A. Processes and imagery of first‐year fast sea ice during the melt season. Journal of Geophysical Re-search: Oceans. 1985, 90, 5045-62.

Perovich, D.K.; Tucker, W.B. Arctic sea-ice conditions and the distribution of solar radiation during summer. Ann. Glaciol. 1997, 25, 445-50.

Rothrock, D.A.; Thorndike, A.S. Measuring the sea ice floe size distribution. Journal of Geophysical Research: Oceans. 1984, 89, 6477-86.

Sudakow, I.; Asari, V.K.; Liu, R.; Demchev, D. MeltPondNet: A Swin Transformer U-Net for Detection of Melt Ponds on Arctic Sea Ice. Ieee J. Sel. Top. Appl. Earth Observ. Remote Sens. 2022, 15, 8776-84.

Tschudi, M.A.; Curry, J.A.; Maslanik, J.A. Airborne observations of summertime surface features and their effect on sur-face albedo during FIRE/SHEBA. Journal of Geophysical Research: Atmospheres. 2001, 106, 15335-44.

Tschudi, M.A.; Curry, J.A.; Maslanik, J.A. Determination of areal surface-feature coverage in the Beaufort Sea using air-craft video data. Ann. Glaciol. 1997, 25, 434-8.

Alekseeva, T.A.; Frolov, S.V. Comparative analysis of satellite and shipborne data on ice cover in the Russian Arctic seas. Izvestiya, Atmospheric and Oceanic Physics. 2013, 49, 879-85.

Wang, Q.; Li, Z.; Lu, P.; Lei, R.; Cheng, B. 2014 summer Arctic sea ice thickness and concentration from shipborne obser-vations. 2018.

Panchi, N.; Kim, E.; Bhattacharyya, A. Supplementing Remote Sensing of Ice: Deep Learning-Based Image Segmentation System for Automatic Detection and Localization of Sea-ice Formations From Close-Range Optical Images. Ieee Sens. J. 2021, 21, 18004-19.

Haverkamp, D.; Soh, L.K.; Tsatsoulis, C. A dynamic local thresholding technique for sea ice classification.:IEEE, 1993,638-40.

Soh, L.; Tsatsoulis, C.; Stein, T.I. Automated Sea Ice Segmentation (ASIS). Ieee International Geoscience and Remote Sensing Symposium Proceedings. 1998, 1998, 586-8.

Kim, J.G.; Hunke, E.C.; Lipscomb, W.H. Sensitivity analysis and parameter tuning scheme for global sea-ice modeling. Ocean Model. 2006, 14, 61-80.

Lu, P.; Leppäranta, M.; Cheng, B.; Li, Z.; Istomina, L.; Heygster, G. The color of melt ponds on Arctic sea ice. The Cry-osphere. 2018, 12, 1331-45.

Perovich, D.K.; Tucker, W.B.; Ligett, K.A. Aerial observations of the evolution of ice surface conditions during summer. Journal of Geophysical Research: Oceans. 2002, 107, 21-4.

Inoue, J.; Curry, J.A.; Maslanik, J.A. Application of Aerosondes to Melt-Pond Observations over Arctic Sea Ice. J. Atmos. Ocean. Technol. 2008, 25, 327-34.

Huang, W.; Lu, P.; Lei, R.; Xie, H.; Li, Z. Melt pond distribution and geometry in high Arctic sea ice derived from aerial investigations. Ann. Glaciol. 2016, 57, 105-18.

Knuth, M.A.; Ackley, S.F. Summer and early-fall Sea-ice concentration in the Ross Sea: comparison of in Situ ASPeCt ob-servations and satellite passive microwave estimates. Ann. Glaciol. 2006, 44, 303-9.

Li, L.; Ke, C.; Xie, H.; Lei, R.; Tao, A. Aerial observations of sea ice and melt ponds near the North Pole during CHINA-RE2010. Acta Oceanol. Sin. 2017, 36, 64-72.

Renner, A.H.H.; Dumont, M.; Beckers, J.; Gerland, S.; Haas, C. Improved characterisation of sea ice using simultaneous aerial photography and sea ice thickness measurements. Cold Reg. Sci. Tech. 2013, 92, 37-47.

Wright, N.C.; Polashenski, C.M. Open-source algorithm for detecting sea ice surface features in high-resolution optical im-agery. The Cryosphere. 2018, 12, 1307-29.

Miao, X.; Xie, H.; Ackley, S.F.; Perovich, D.K.; Ke, C. Object-based detection of Arctic sea ice and melt ponds using high spatial resolution aerial photographs. Cold Reg. Sci. Tech. 2015, 211-22.

Lu, P.; Li, Z. A method of obtaining ice concentration and floe size from shipboard oblique sea ice images. Ieee Trans. Ge-osci. Remote Sensing. 2010, 48, 2771-80.Beltaos S. and Burrell B.C., 2015, Hydrotechnical advances in Canadian river ice science and engineering during the past 35 years. Canadian Journal of Civil Engineering, 42, p. 583 591.